Computational design of metallohydrolases

https://doi.org/10.1038/s41586-025-09746-w

Received: 12 November 2024

Accepted: 13 October 2025

Published online: 03 December 2025

Open access

Check for updates

Donghyo Kim[1,2,10], Seth M. Woodbury[1,2,3,10], Woody Ahern[1,2,4,10], Doug Tischer[1,2], Alex Kang[1,2], Emily Joyce[1,2], Asim K. Bera[1,2], Nikita Hanikel[1,2], Saman Salike[1,2,5], Rohith Krishna[1,2], Jason Yim[6], Samuel J. Pellock[1,2], Anna Lauko[1,2,7], Indrek Kalvet[1,2,8] ✉, Donald Hilvert[9] ✉ & David Baker[1,2,8] ✉

De novo enzyme design seeks to build proteins containing ideal active sites with catalytic residues surrounding and stabilizing the transition state(s) of the target chemical reaction[1–7]. The generative artificial intelligence method RFdiffusion[8,9] solves this problem, but requires specifying both the sequence position and backbone coordinates for each catalytic residue, limiting sampling. Here we introduce RFdiffusion2, which eliminates these requirements, and use it to design zinc metallohydrolases starting from quantum chemistry-derived active site geometries. From an initial set of 96 designs tested experimentally, the most active has a catalytic efficiency (k_{cat}/K_M) of 16,000 M^{-1} s^{-1}, orders of magnitude higher than previously designed metallohydrolases[6,7,10,11]. A second round of 96 designs yielded 3 additional highly active enzymes, with k_{cat}/K_M values of up to 53,000 M^{-1} s^{-1} and a catalytic rate constant (k_{cat}) of up to 1.5 s^{-1}. The design models of the four most active designs differ from known structures and from each other, and the crystal structure of the most active design is very close to the design model, demonstrating the accuracy of the design method. The most active enzymes are predicted by PLACER[12] and Chai-1 (ref. 13) to have preorganized active sites that effectively position the substrate for nucleophilic attack by a water molecule activated by the bound metal. The ability to generate highly active enzymes directly from the computer, without experimental optimization, should enable a new generation of potent designer catalysts[14,15].

Metallohydrolases catalyse some of the most difficult hydrolysis reactions in biology by using their bound metal ions to activate a water molecule positioned adjacent to the substrate bond to be cleaved[16–18]. Engineering new metallohydrolases is currently of considerable interest for degrading human-generated environmental pollutants, for which there has not been sufficient time for efficient hydrolytic enzymes to evolve[19–21]. Protein engineering has expanded the scope of substrates that can be hydrolysed by metallohydrolases, but this often requires initial promiscuous activity[22,23]. De novo enzyme design has been used to generate new metallohydrolases[6,10,24], but these have had relatively low activity and efficiency, and have required extensive directed evolution to match the activity and efficiency of native enzymes[24]. Given an ideal metallohydrolase active site, de novo enzyme design seeks to identify or generate a protein scaffold that positions the catalytic residues, metals, and substrates in optimal catalytic geometries with high accuracy[25,26]. RFdiffusion has been used successfully to scaffold active sites, but the search has been limited by the need to specify the sequence positions and conformations of the catalytic residues[8,9,27].

We reasoned that a generative artificial intelligence design method that only required the specification of side-chain functional group positions around a reaction transition state, and was capable of sampling over all possible sequence positions and conformations of these residues, could more readily satisfy complex catalytic constraints[14,15,28,29]. We set out to develop such an approach, and used it to design new metallohydrolases starting from a quantum chemistry-generated active site description with a bound metal cofactor.

To enable sequence-position and side-chain rotamer-agnostic enzyme design, we developed a generative artificial intelligence flow-matching model called RFdiffusion2[30]. RFdiffusion2 extends the capabilities of RFdiffusion to generate scaffolds that position a set of functional residues (a 'motif') in two key ways. First, it enables atomic substructure scaffolding: RFdiffusion can only scaffold backbone-level motifs (with the side-chain and backbone atom N-Cα-C=O positions specified), whereas RFdiffusion2 can scaffold arbitrary atom-level motifs (any subset of amino acid heavy atoms). This is important for enzyme design because it allows users to specify only the positions of the key functional groups that interact with the reaction transition state, rather than the full side-chain and backbone conformation. Second, RFdiffusion2 enables sequence-position-agnostic scaffolding: RFdiffusion requires specification of the primary sequence positions of the motif residues, but RFdiffusion2 can scaffold motifs whose primary sequence positions are unknown. RFdiffusion2 replaces diffusion with flow matching[31,32] and achieves sequence-position-agnostic atomic substructure scaffolding by providing randomly selected native atomic coordinates (but not their sequence positions) during training in addition to the partially noised, sequence-labelled atomic coordinates. With these improvements, RFdiffusion2 generates diverse proteins starting directly from catalytic configurations that consist of input

[1]Department of Biochemistry, University of Washington, Seattle, WA, USA. [2]Institute for Protein Design, University of Washington, Seattle, WA, USA. [3]Graduate Program in Bioengineering, University of Washington, Seattle, WA, USA. [4]Paul G. Allen School of Computer Science and Engineering, University of Washington, Seattle, WA, USA. [5]Graduate Program in Chemical Engineering, University of Washington, Seattle, WA, USA. [6]Massachusetts Institute of Technology, Cambridge, MA, USA. [7]Graduate Program in Biological Physics, Structure and Design, University of Washington, Seattle, WA, USA. [8]Howard Hughes Medical Institute, University of Washington, Seattle, WA, USA. [9]Laboratory of Organic Chemistry, ETH Zurich, Zurich, Switzerland. [10]These authors contributed equally: Donghyo Kim, Seth M. Woodbury, Woody Ahern. ✉e-mail: ikalvet@uw.edu; hilvert@ethz.ch; dabaker@uw.edu

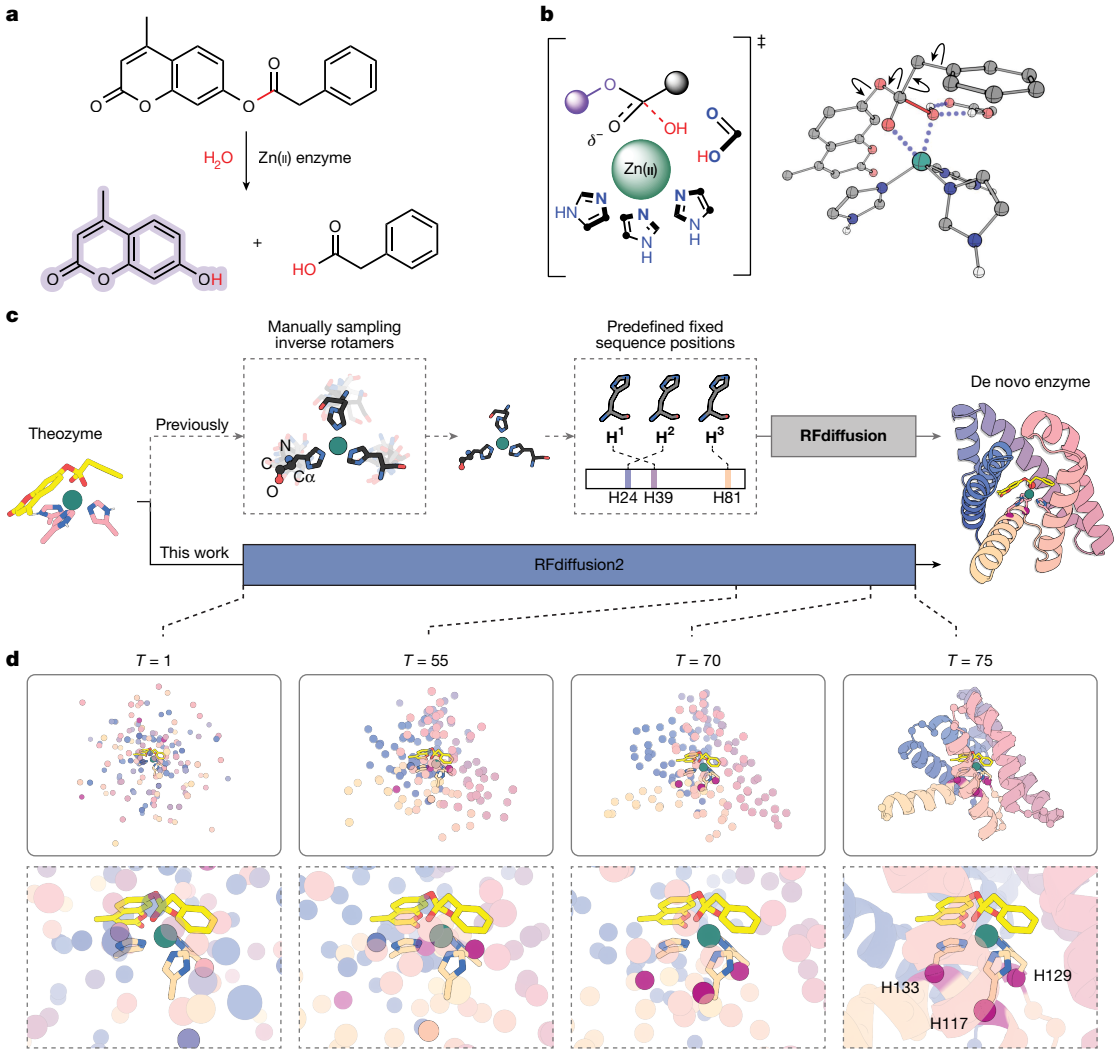

Fig. 1 | RFdiffusion2 design method. a, Hydrolysis of 4MU-PA yields phenylacetic acid and a fluorescent coumarin product. **b**, Example theozyme for Zn(II)-hydroxide nucleophilic attack on the 4MU-PA ester. Two-dimensional representation (left) and 3D DFT model (right). Arrows on the 3D model represent sampled conformational flexibility. **c**, Comparison of scaffold generation around an input theozyme using previous backbone centric RFdiffusion (top row) versus interaction functional group centric RFdiffusion2. RFdiffusion requires explicit upfront sampling of side-chain conformations and residue sequence positions, whereas RFdiffusion2 only requires the transition-state complex and the catalytic side-chain functional groups, implicitly sampling sequence space and rotameric space during inference. **d**, Snapshots of the global structure and active site from model X_T during an RFdiffusion2 inference trajectory. The coordinates of the input transition-state complex and catalytic functional groups stay fixed during inference while the backbone structure, sequence positions, and unspecified atoms of the catalytic side chains are sampled by RFdiffusion2. The Cα atoms that host the catalytic histidines at the end of the trajectory are retrospectively highlighted as red spheres; these Cα atoms are not predetermined but rather move into the frame to host the fixed side chains as the global structure forms around the motifs.

functional group positions and substrate coordinates. Allowing the model to resolve the a priori unknown degrees of freedom (that is, the primary sequence positions and side-chain rotamer conformations of the catalytic residues) is considerably more effective at generating self-consistent design solutions than randomly sampling those degrees of freedom before inference, because the space is far too large to enumerate, as was necessitated with RFdiffusion. A detailed description of RFdiffusion2 training and benchmarking results for a wide range of active site scaffolding problems is described elsewhere[30].

As an initial test of RFdiffusion2, we chose to design a zinc metallohydrolase for the hydrolysis of a fluorogenic ester, 4-methylumbelliferyl phenylacetate (4MU-PA), as a target reaction (Fig. 1a). We began by using density functional theory (DFT) to identify the transition-state geometry of the rate-determining Zn(II)-OH nucleophilic attack on the substrate ester. Four distinct catalytic arrangements based on the stereochemistry of the tetrahedral intermediate and the nature of the oxyanion hole were considered (Fig. 1b, Supplementary Figs. 1 and 2, Supplementary Data 1 and Supplementary Methods 4.1). These calculations provide the coordinates of the three Zn(II)-binding imidazole rings, the metal, and the transition state. Our previous RFdiffusion approach required the backbone coordinates and residue positions as inputs, which would require upfront sampling of the rotameric states and sequence position for each histidine. This cannot be done exhaustively: even with relatively coarse sampling around the side-chain chi angles χ_1, χ_2, and the backbone torsion angle ψ, there are on the order of 10^{18} possible choices for the side-chain conformations and sequence placements of our full catalytic site (Fig. 1c and Extended Data Fig. 1). Whereas each RFdiffusion run has to be initialized with a specific (and generally randomly selected) choice from this enormous set of combinations, RFdiffusion2 as described above searches the entire space in each trajectory.

RFdiffusion2 inference trajectories were used to build protein scaffolds housing the DFT-generated minimal active site configurations, referred to as theozymes[2,33]. Several snapshots from a representative

trajectory are shown in Fig. 1d, transforming random noise on the left into the final backbone on the right (Supplementary Video 1). The Cα atoms of each residue (shown as coloured spheres representing final sequence position) are initially sampled from a Gaussian distribution, and the target functional atom positions (shown in sticks) stay fixed. As the trajectory proceeds from left to right, the global structure takes shape around the motif, with the fixed histidine side chains eventually connecting to Cα atoms of the protein backbone at sequence positions of the network's choosing. A total of 5,120 RFdiffusion2 inference trajectories were carried out starting from different random seeds and for each of the resulting protein scaffolds, sequences were generated using ProteinMPNN[34]. The catalytic geometry and interactions with the transition state of those designs for which the AlphaFold2[35] predicted structure was close to the design model were further optimized using iterative LigandMPNN[36] and constrained Rosetta repacking and minimization[37] (Extended Data Fig. 2 and Supplementary Methods 4.1). Designs containing a proposed general base positioned to activate the water molecule (that is, Glu, Asp or His within hydrogen bonding distance of the Zn(II)-bound water) and side-chain hydrogen bonds stabilizing the transition-state oxyanion (if applicable), and that AlphaFold2 predicted to adopt the target structure, were characterized with PLACER[12] to assess active site preorganization. A total of 96 designs were selected for experimental characterization on the basis of predicted active site geometry and preorganization (Supplementary Fig. 3, Supplementary Data 2 and 3 and Supplementary Methods 4.1).

Linear DNA fragments encoding the 96 designs were cloned into a plasmid encoding a C-terminal Strep-tag and used to transform *Escherichia coli*, and the resulting proteins were purified using Strep-tag affinity chromatography. Eighty-six out of ninety-six designs were expressed and soluble as judged by SDS–PAGE analysis of the eluants (Supplementary Fig. 4). Purified designs were supplemented with zinc sulfate, and hydrolysis of 4MU-PA was monitored by fluorescence. Five designs (A1, A8, B9, C4 and F7) had activity well above background (Fig. 2b and Supplementary Fig. 5). Sequence-verified single clones for each of these were expressed and purified by affinity chromatography followed by size-exclusion chromatography to obtain pure, monomeric protein fractions (Supplementary Figs. 6 and 7 and Supplementary Table 1). Michaelis–Menten kinetic characterization of the purified variants revealed a k_{cat}/K_M of 16,000 ± 2,000 M^{-1} s^{-1} for A1, the most active design, and k_{cat}/K_M values in the range of 35–140 M^{-1} s^{-1} for the other four designs (Fig. 2c,d, Extended Data Fig. 3 and Extended Data Table 1). For comparison, the k_{cat}/K_M of previously designed metallohydrolases[24] ranged from 3 to 60 M^{-1} s^{-1} (Supplementary Table 2). A1 is also a relatively robust enzyme, and retains activity for at least 1,000 turnovers (Fig. 3e and Supplementary Fig. 8). A1 differs considerably from previously described proteins: the most similar structures identified through template modelling (TM) alignment with the Protein Data Bank (PDB) and AlphaFold Protein Structure Database (AFDB) have TM scores[38] of 0.41 and 0.49, respectively, and do not have analogous arrangements of catalytic residues (Extended Data Fig. 4a,b). We refer to A1 as zinc metalloesterase 1 (ZETA_1) throughout the remainder of the text.

Design ZETA_1 not only has remarkably high activity but was also the top-ranked design in our in silico ranking. The structure in the absence of substrate was predicted to be very close to the design model by AlphaFold2 (Extended Data Fig. 5a and Supplementary Figs. 9 and 10), and the designed active site of ZETA_1 was predicted to be highly preorganized by PLACER, with the catalytic side chains fixed in place and the substrate held closely in its designed position, adjacent to the proposed Zn(II) site. PLACER[12] is a deep neural network that, given a protein backbone containing a substrate, fully randomizes the positions of the substrate and all side chains within a 600-atom sphere, and then generates new coordinates for these groups[12]; repeated PLACER trajectories generate an ensemble of possible side-chain conformations and small molecule docks. Design ZETA_1 stood out from the other designs in both the extent of catalytic site preorganization (the catalytic side chains were largely fixed in space in catalytically competent conformations) and the positioning of the substrate–transition state in the active site (in the ZETA_1 ensemble, the substrate remained largely fixed in space in the active site, whereas in the inactive designs H7 and H8, it fluctuated considerably) (Fig. 2e–h and Supplementary Videos 2–5). Seven designs based on the same ZETA_1 backbone family were initially filtered out during the design selection phase, as they had suboptimal PLACER metrics; we retrospectively expressed and purified these designs and found that they had very low or no activity, further highlighting the utility of PLACER ensemble calculations for identifying active designs (Supplementary Fig. 11). These findings suggest that combining global structure prediction with detailed PLACER modelling of the active site provides a powerful approach to assessing the catalytic machinery and substrate binding geometry for design selection (Supplementary Fig. 10).

The ZETA_1 active site consists of a primarily hydrophobic pocket with three histidines binding Zn(II) with their Nε atoms, an aspartate as a potential general base, and an asparagine that forms a hydrogen bond to the coumarin ring (Fig. 3a). As in the original theozyme model used to generate ZETA_1, the Zn(II) ion also acts as an oxyanion hole, stabilizing the developing negative charge at the transition state; there are no nearby side-chain hydrogen bond donors (Extended Data Fig. 5). Zinc is absolutely critical for ZETA_1 activity: extraction of bound Zn(II) by dialysis in the presence of the chelator 1,10-phenanthroline completely eliminated activity, and activity was subsequently restored by addition of zinc to the solution (Fig. 3f). Zinc titration experiments measured a dissociation constant (K_D) for Zn(II) of 41 ± 5 nM, which is similar to those of previous designed zinc enzymes[26,39], but higher than native zinc hydrolases[18,40–42], which typically have K_D values less than 10 nM.

We carried out mutagenesis experiments to probe the contributions of the designed catalytic residues to Zn(II)-binding and catalysis (Fig. 3g–i and Supplementary Figs. 12–14). In the design model, N17 positions the substrate by hydrogen bonding with the lactone carbonyl of the coumarin moiety and could stabilize the developing negative charge on the leaving group; the N17A mutation led to a 8.1-fold decrease in k_{cat}/K_M (Supplementary Fig. 13). Mutation of all three metal-coordinating histidine residues to alanine simultaneously (H118A/H130A/H134A), as well as two of the three single histidine-to-alanine substitutions (H118A/H134A), completely inactivated the enzyme, as expected. Mutating the third Zn(II)-coordinating residue to alanine (H130A) resulted in a decrease of only 13-fold in k_{cat}/K_M, and mutation of the proposed general base D67 to alanine had little effect on k_{cat}/K_M and increased Zn(II)-binding affinity. These results suggest that H134/H118/H130 and H134/H118/D67 may be competing Zn(II)-binding sites owing to the close proximity of the coordinating side chains of H130 and D67, which was corroborated by Chai-1 (ref. 13) predictions of the protein–Zn(II)–substrate complex (Extended Data Fig. 5b,c); the D67A mutation may confine the zinc to the originally designed coordination sphere with the three histidines, which is more catalytically competent. In the H130A mutant, D67 is likely to coordinate Zn(II) and maintain binding, albeit in a less optimal binding geometry, lowering the zinc affinity and enzyme activity.

Guided by these observations, we started from new DFT theozymes explicitly containing the catalytic base, and generated protein structures scaffolding these theozymes using a newer version of RFdiffusion2 trained from random weight initialization on a threefold-larger dataset (previous versions were fine-tuned from structure prediction weights) (Fig. 4a, Supplementary Data 1 and Supplementary Methods 4.2). Designs whose Chai-1 predictions of the protein–Zn(II)–substrate phosphonate ester complex, mimicking the reaction transition state, closely matched the design models with high confidence were identified by PLACER to have highly preorganized active sites (Supplementary Figs. 15 and 16). Ninety-six such designs spanning 37 RFdiffusion2-generated backbones were selected for experimental

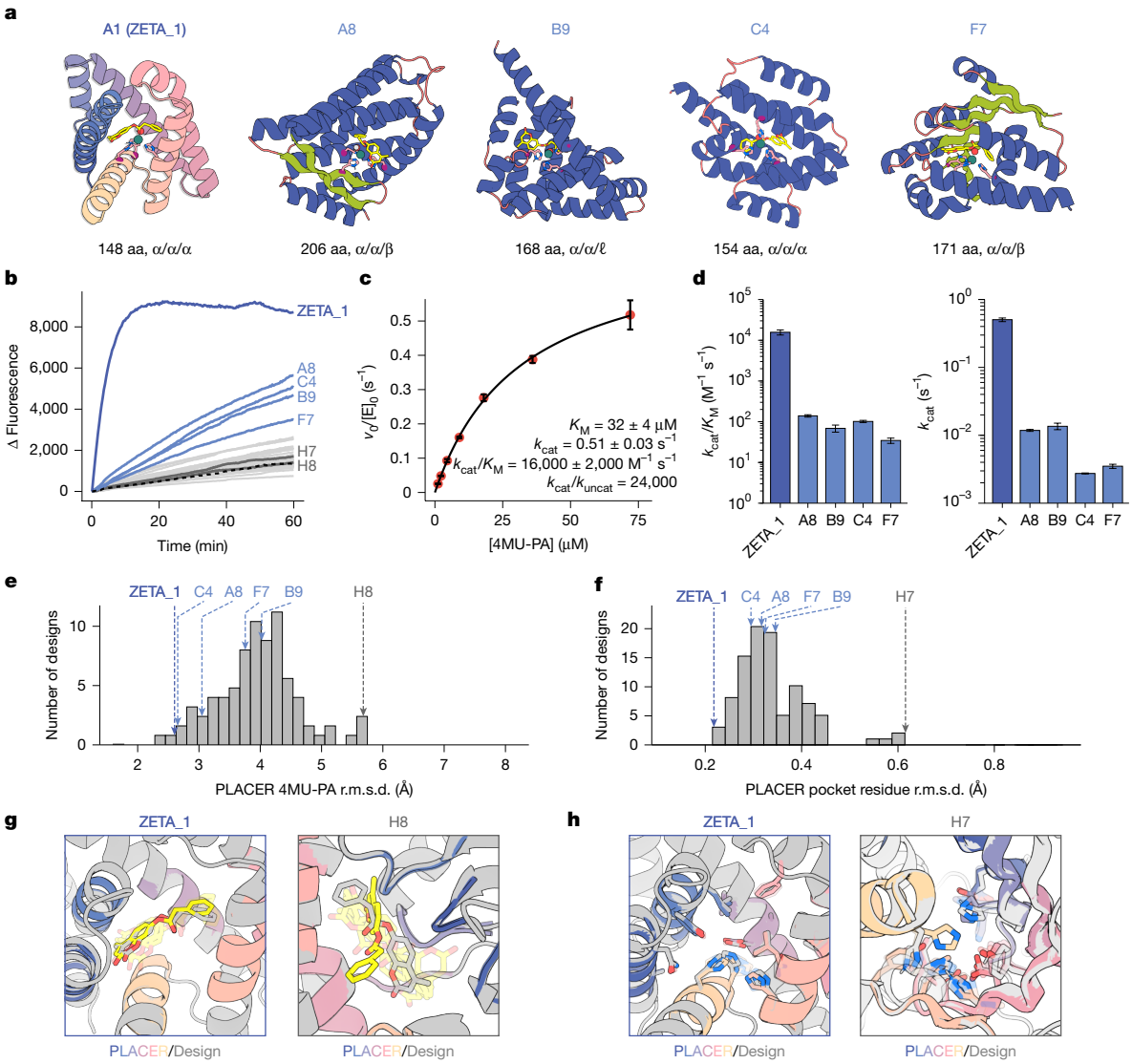

Fig. 2 | Activity characterization and PLACER preorganization assessment. **a**, Design models of the most active designs. Sequence length (in amino acids (aa)) and the secondary structure harbouring each catalytic histidine are indicated below. **b**, Reaction progress curves. The dashed black line is the buffer background. **c**, Michaelis–Menten characterization of A1 (ZETA_1). The *y* axis shows the initial rate v_0 divided by the total enzyme concentration ($[E]_0$). **d**, Michaelis–Menten parameters of most active designs. **e**,**f**, Distribution of PLACER active site preorganization ensemble metrics for the ordered designs. Average design-prediction substrate r.m.s.d. (**e**) and average catalytic and binding residue design-prediction r.m.s.d. (**f**) across all predicted ensembles generated by PLACER for each design. **g**, For ZETA_1, the substrate position in PLACER ensembles is close to the design model, whereas in the inactive design H7, the substrate position fluctuates widely. **h**, For ZETA_1, the side chains surrounding the active site are largely fixed in positions close to the original design model, whereas in the inactive H8 design, the side-chain positions vary considerably. Note that only the first five randomly generated, unranked ensemble predictions are shown for PLACER in **g**,**h**. Data represent the mean ± s.d. of three independent measurements of initial velocity (**c**) and Michaelis–Menten parameters (**d**).

characterization (Supplementary Fig. 17 and Supplementary Data 2 and 3). Eighty-five of the 96 designs were expressed and soluble (Supplementary Fig. 18), and 11 designs spanning 3 different folds had substantial zinc-dependent 4MU-PA hydrolysis activity (Fig. 4b,c and Supplementary Fig. 19). Michaelis–Menten analysis revealed that 5 designs had a k_{cat}/K_M greater than 10^4 M^{-1} s^{-1} and 6 designs had a k_{cat}/K_M greater than 10^3 M^{-1} s^{-1} (Fig. 4d, Extended Data Fig. 6 and Extended Data Table 1). The most active designs for each backbone had a k_{cat}/K_M = 53,000 ± 5,000 M^{-1} s^{-1} (ZETA_2), k_{cat}/K_M = 19,000 ± 2,000 M^{-1} s^{-1} (ZETA_3), and k_{cat}/K_M = 1,100 ± 200 M^{-1} s^{-1} (ZETA_4) (Fig. 4f–h and Supplementary Fig. 20). ZETA_2 has a k_{cat} = 1.5 ± 0.1 s^{-1}, a threefold increase over the k_{cat} of ZETA_1, and close to that of the metallohydrolase MID1sc10 obtained after 10 rounds of directed evolution[24]. RFdiffusion2 enables specification of the position of the substrate relative to the centre of mass of the designed protein; for ZETA_2 and ZETA_3, the protein was centred near the phenylacetate and 4-methylumbelliferyl moieties, respectively, of 4MU-PA, resulting in opposite substrate binding modes in the design models (that is, the 4-methylumbelliferyl is exposed in ZETA_2 and the phenylacetate is exposed in ZETA_3) (Extended Data Fig. 7).

The success rate in the second design campaign was considerably higher than the first campaign (11 out of 96 versus 1 out of 96 designs with k_{cat}/K_M greater than 10^3 M^{-1} s^{-1}), supporting the conclusions from the first round analysis (Supplementary Figs. 21–26, Supplementary Table 3, Supplementary Discussion 2 and Supplementary Methods 4.2). Circular dichroism experiments confirmed that all active enzyme scaffolds from both design campaigns possess secondary structures consistent with their design models, indicating proper folding (Supplementary Fig. 21). The structures of ZETA_1-4 are rather different from each other and previously known metallohydrolases (Extended Data Fig. 4).

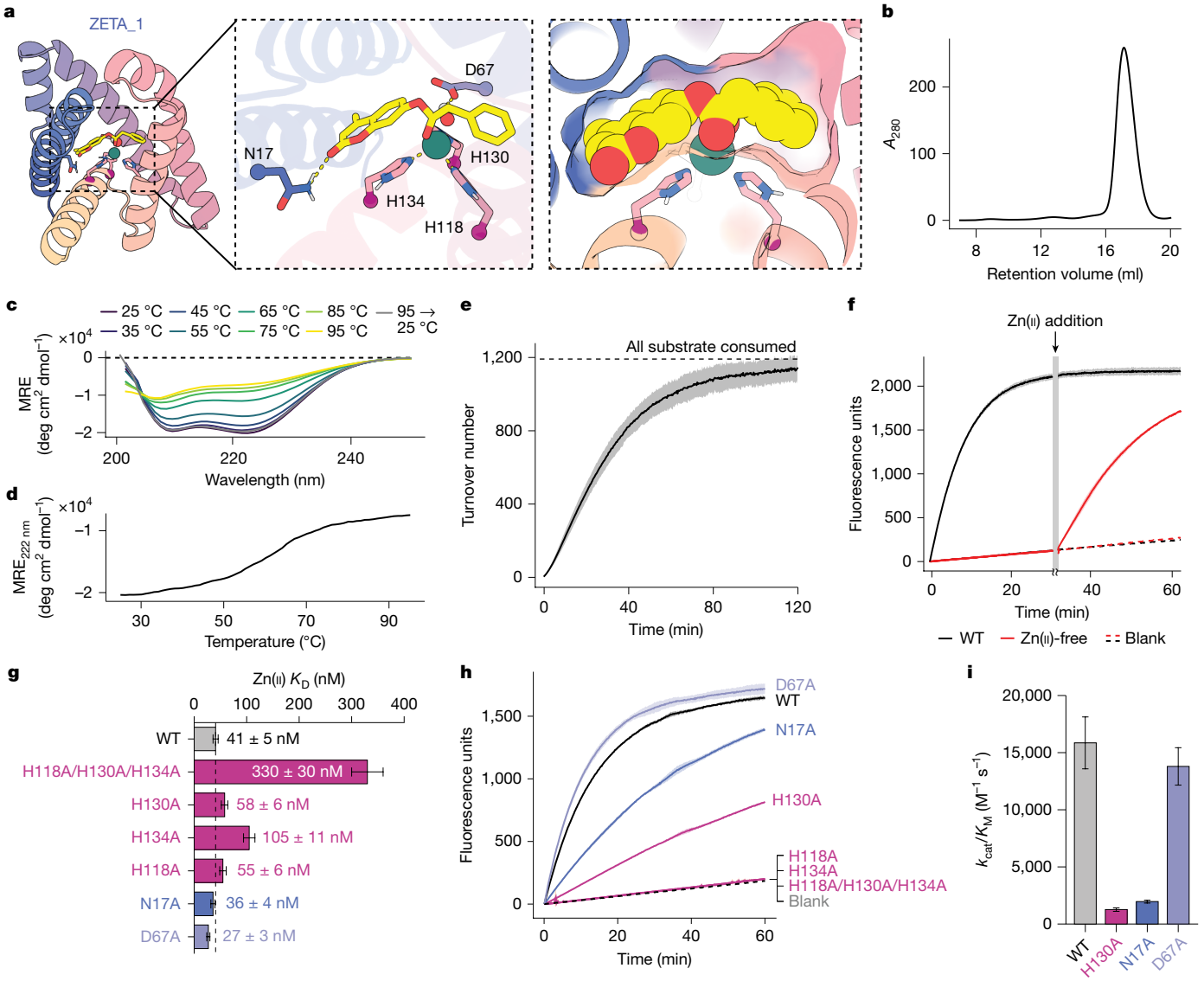

Fig. 3 | Characterization of ZETA_1 activity. a, ZETA_1 design model (left) with close-up view of the active site showing the catalytic residues (middle) and a surface view of the designed pocket revealing high shape-complementarity to the substrate (right). **b**, Size-exclusion chromatogram of ZETA_1 showing a single peak corresponding to monomeric protein. **c**, Circular dichroism spectra of ZETA_1 recorded every 10 °C from 25 °C to 95 °C (viridis colour gradient), and after recooling to 25 °C (grey). The spectra suggest that ZETA_1 has an α-helical secondary structure and that it can refold after heating and partial unfolding. MRE, mean residue ellipticity. **d**, Circular dichroism signal at 222 nm measured every 1 °C and plotted as a function of temperature. **e**, [Product]:[enzyme] progress curve shows that ZETA_1 hydrolyses more than 1,000 4MU-PA molecules per enzyme. Note that the background reaction has been subtracted from the spectra so that every turnover can be attributed to the enzyme (Supplementary Fig. 8; further details in Supplementary Information, section 4.3). **f**, Reaction progress curves for the Zn(II) holo- and zinc-free apo ZETA_1 proteins showing zinc-dependent activity. Adding excess Zn(II) to the apo ZETA_1 sample after 30 min re-establishes the activity, demonstrating that zinc is essential for the catalytic mechanism of ZETA_1. WT, wild type. **g**, Zinc affinity of wild-type and mutant ZETA_1, measured as the dissociation constant (K_D), where a lower value indicates tighter binding. **h**, Fluorescence progress curves comparing the activity of wild-type and mutant ZETA_1. **i**, k_{cat}/K_M for active ZETA_1 mutants compared with the wild type. Data represent the mean ± s.d. of three independent measurements of turnover number (**e**), fluorescence progress curves (**f**,**h**), Zn(II)-binding dissociation constant (**g**) and Michaelis–Menten parameters (**i**).

The sequence positions of the catalytic residues in each of these enzymes are also very different, highlighting the diversity of RFdiffusion2 generated design solutions (Fig. 4c and Supplementary Tables 4 and 5).

We determined the structure of ZETA_2, the most active design, in the apo state at 3.5 Å using X-ray crystallography (PDB: 9PYJ; Fig. 5). The experimental structure is in good agreement with the design model, with nearly superimposable backbones (Cα root mean squared deviation (r.m.s.d.) = 1.1 Å) and the catalytic residues preorganized in the designed geometry (Fig. 5a,b). The binding pocket is complementary to the superimposed transition state from the design model (Fig. 5c). We also solved a 2.1 Å structure after soaking ZETA_2 in Zn(II) (PDB: 9PYL; Extended Data Fig. 8); whereas the backbone was again nearly superimposable with the design model (Cα r.m.s.d. = 0.8 Å) and a Zn(II) ion was present with 100% occupancy at the designed location (r.m.s.d. = 1.7 Å), one of the Zn(II)-coordinating histidines (H110) was flipped out to interact with a Zn(II) ion bound at the surface of the protein, probably because of the high Zn(II) concentration in the crystal soaking buffer (250 mM) (Extended Data Fig. 8).

Conclusion

Here we demonstrate that RFdiffusion2 can generate highly active metallohydrolases directly from active site configurations obtained by quantum chemistry calculations. The zero-shot design of an enzyme

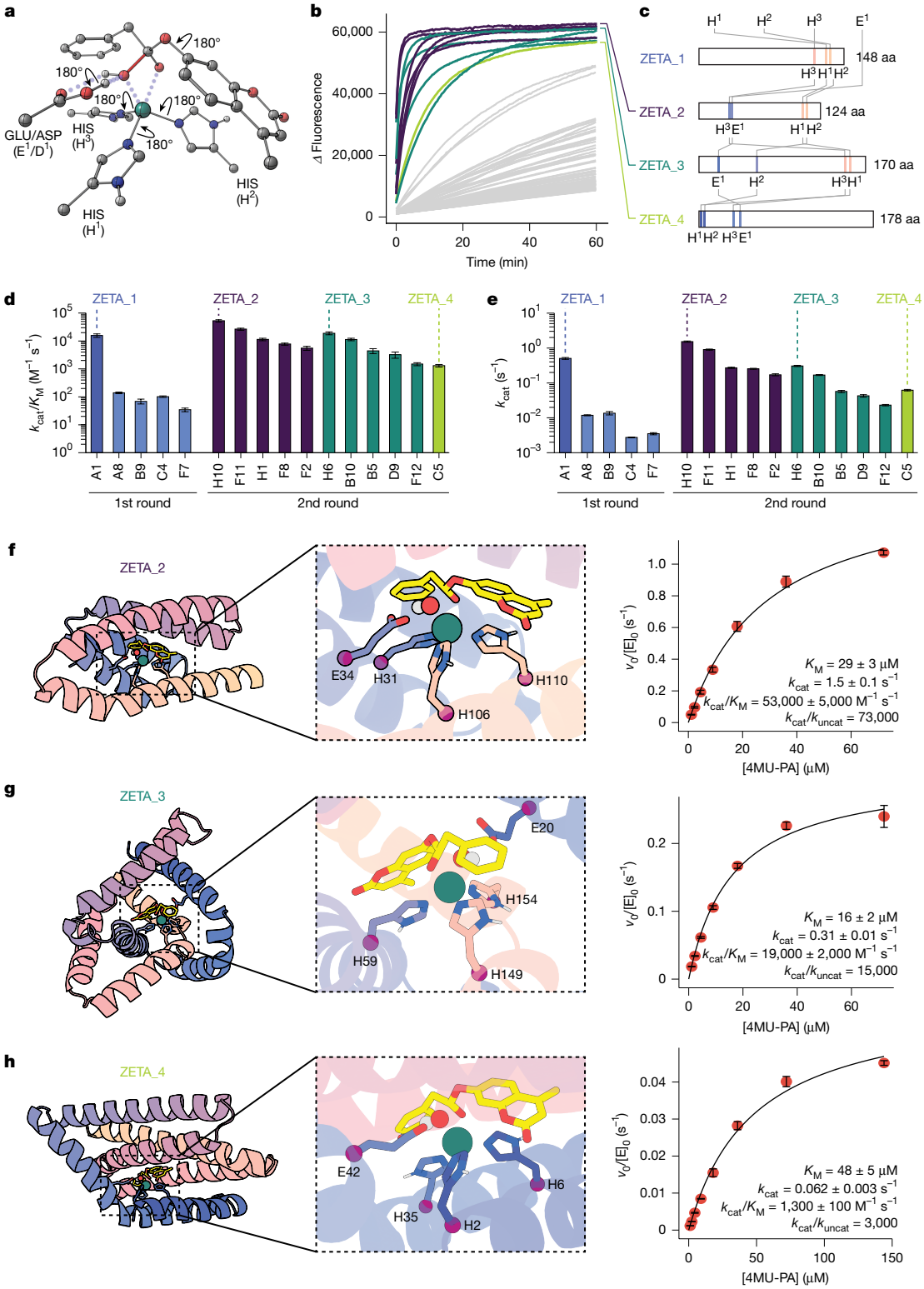

Fig. 4 | Characterization of second round designs. a, Second round DFT theozymes containing the catalytic base. Zn(II) is coordinated by the His Nε atoms in these theozymes, and thus C_β is explicitly modelled. **b**, Reaction progress curves coloured by scaffold family. **c**, Sequence length and catalytic residue positioning for the top design in each scaffold, named ZETA_2-4. These designs differ from each other and from ZETA_1. **d**,**e**, Steady-state k_{cat}/K_M and k_{cat} parameters for the 11 second round hits, with colours corresponding to scaffolds using the scheme in **b**,**c**. Activities are higher, on average, than in the first round of designs (blue). **f**–**h**, Design model (left) with close-up view of the active site (middle) for ZETA_2 (**f**), ZETA_3 (**g**) and ZETA_4 (**h**). Right, Michaelis–Menten plots and parameters. Data represent the mean ± s.d. of three independent measurements of Michaelis–Menten parameters (**d**,**e**) and initial velocity (**f**–**h**).

(ZETA_1) with a k_{cat}/K_M greater than 10^4 M^{-1} s^{-1}—the top-ranked in silico design out of a total of 96 tested straight from the computer, with no experimental optimization—is a considerable advance for de novo enzyme design, which has previously required extensive design screening and directed evolution to achieve activities at this level[14,24]. The robustness of our design strategy is demonstrated by the zero-shot

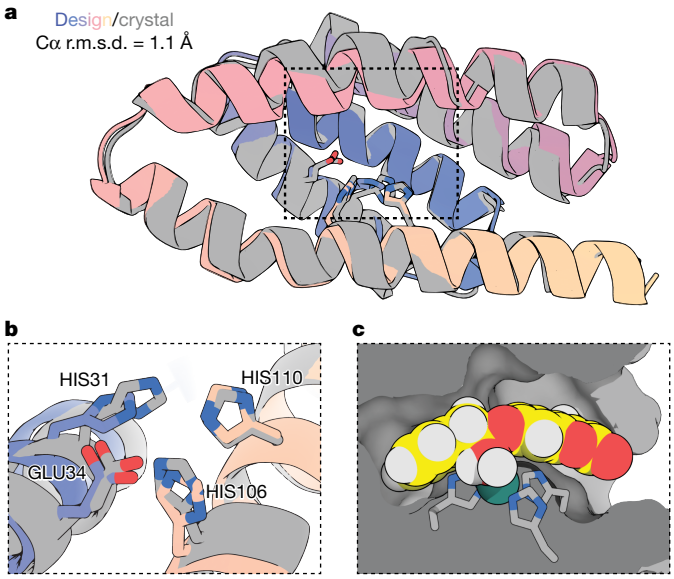

Fig. 5 | Crystal structure of ZETA_2 closely resembles the design model. **a**, Cα superposition of the design model and the X-ray crystal structure of ZETA_2 (PDB: 9PYJ) in the apo state, resolved at 3.5 Å resolution. Catalytic residues are shown as sticks. The structures are in close agreement (Cα r.m.s.d. = 1.1 Å) and the catalytic residues in the experimental structure are preorganized close to their designed catalytic geometry. **b**,**c**, Magnification of the active site of ZETA_2, highlighting the agreement between the experimental and designed catalytic geometry (**b**) and the shape-complementarity of the designed binding pocket and the transition state model (superimposed in from the design model) (**c**). The crystal structure is shown in grey and the design model is in colour in all panels.

design of 3 additional enzymes from a new set of 96 designs tested straight from the computer: ZETA_2 and ZETA_3, with a k_{cat}/K_M of more than $10^4\,M^{-1}\,s^{-1}$, and ZETA_4, with a k_{cat}/K_M greater than $10^3\,M^{-1}\,s^{-1}$. ZETA_1–4 have structures that are very different from each other and from previously known structures. The catalytic efficiencies of ZETA_1–3 are within the range typically observed for native metallohydrolases with similar substrates ($k_{cat}/K_M = 10^4 \sim 10^6\,M^{-1}\,s^{-1}$) and greater than for all previously designed metallohydrolases prior to optimization[43–47] (Supplementary Table 2). Experimental characterization of ZETA_1 and ZETA_2 provide strong evidence that they function as designed, utilizing a bound Zn(II) ion to activate a water molecule for nucleophilic attack and to stabilize the resulting oxyanion intermediate and flanking transition states. The results from PLACER and the Chai-1 ensembles suggest that the key to obtaining k_{cat}/K_M of over $10^4\,M^{-1}\,s^{-1}$ is precise substrate placement relative to the activated water and the Zn(II) ion. Future metallohydrolase design efforts that: (1) position the general base such that it cannot reconfigure to interact with the bound metal ion (as in the case of ZETA_1); (2) better preorganize the metal-binding residues; and (3) incorporate further side-chain oxyanion stabilization, could increase activity to levels comparable to the most active native metallohydrolases.

Our RFdiffusion2–PLACER design approach has many advantages over previous de novo enzyme design methods and should be broadly applicable for generating efficient catalysts for a wide diversity of chemical reactions. By enabling direct scaffolding of side-chain functional groups, rather than backbone N-Cα-C=O coordinates as required in enzyme design calculations with RFdiffusion[1,27], RFdiffusion2 bypasses the need for explicit enumeration of catalytic side-chain rotamer conformations and placement of the catalytic residues along the linear sequence—this enables each design trajectory to sample from the enormous space of possibilities rather than being confined to a small subspace. Assessment of active site preorganization and substrate–transition state positioning with PLACER and Chai-1 proved remarkably effective at identifying the most active designs; this result, together with similar observations with de novo designed serine hydrolases[1] and retroaldolases[12], suggests that PLACER and related deep learning approaches will be widely useful for design ranking. In our laboratory, we have found the RFdiffusion2–PLACER design approach described here to yield biocatalysts for a variety of bond-breaking and bond-making chemical reactions, and we look forward to seeing what the broader design community can generate with these tools, which we are making freely available.

Online content

Any methods, additional references, Nature Portfolio reporting summaries, source data, extended data, supplementary information, acknowledgements, peer review information; details of author contributions and competing interests; and statements of data and code availability are available at https://doi.org/10.1038/s41586-025-09746-w.

1. Lauko, A. et al. Computational design of serine hydrolases. *Science* **388**, eadu2454 (2025).
2. Tantillo, D. J., Jiangang, C. & Houk, K. N. Theozymes and compuzymes: theoretical models for biological catalysis. *Curr. Opin. Chem. Biol.* **2**, 743–750 (1998).
3. Siegel, J. B. et al. Computational design of an enzyme catalyst for a stereoselective bimolecular Diels–Alder reaction. *Science* **329**, 309–313 (2010).
4. Yeh, A. H.-W. et al. De novo design of luciferases using deep learning. *Nature* **614**, 774–780 (2023).
5. Röthlisberger, D. et al. Kemp elimination catalysts by computational enzyme design. *Nature* **453**, 190–195 (2008).
6. Zastrow, M. L., Peacock, A. F. A., Stuckey, J. A. & Pecoraro, V. L. Hydrolytic catalysis and structural stabilization in a designed metalloprotein. *Nat. Chem.* **4**, 118–123 (2011).
7. Der, B. S., Edwards, D. R. & Kuhlman, B. Catalysis by a de novo zinc-mediated protein interface: implications for natural enzyme evolution and rational enzyme engineering. *Biochemistry* **51**, 3933–3940 (2012).
8. Watson, J. L. et al. De novo design of protein structure and function with RFdiffusion. *Nature* **620**, 1089–1100 (2023).
9. Krishna, R. et al. Generalized biomolecular modeling and design with RoseTTAFold All-Atom. *Science* **384**, eadl2528 (2024).
10. Rufo, C. M. et al. Short peptides self-assemble to produce catalytic amyloids. *Nat. Chem.* **6**, 303–309 (2014).
11. Song, W. J. & Tezcan, F. A. A designed supramolecular protein assembly with in vivo enzymatic activity. *Science* **346**, 1525–1528 (2014).
12. Anishchenko, I. et al. Modeling protein–small molecule conformational ensembles with PLACER. *Proc. Natl Acad. Sci.* **122**, e2427161122 (2025)
13. Discovery, C. et al. Chai-1: Decoding the molecular interactions of life. Preprint at *bioRxiv* https://doi.org/10.1101/2024.10.10.615955 (2024).
14. Lovelock, S. L. et al. The road to fully programmable protein catalysis. *Nature* **606**, 49–58 (2022).
15. Nam, K., Shao, Y., Major, D. T. & Wolf-Watz, M. Perspectives on computational enzyme modeling: from mechanisms to design and drug development. *ACS Omega* **9**, 7393–7412 (2024).
16. Basile, L. A., Raphael, A. L. & Barton, J. K. Metal-activated hydrolytic cleavage of DNA. *J. Am. Chem. Soc.* **109**, 7550–7551 (1987).
17. Lindskog, S. Structure and mechanism of carbonic anhydrase. *Pharmacol. Ther.* **74**, 1–20 (1997).
18. Lipscomb, W. N. & Sträter, N. Recent advances in zinc enzymology. *Chem. Rev.* **96**, 2375–2434 (1996).
19. Chamas, A. et al. Degradation rates of plastics in the environment. *ACS Sustain. Chem. Eng.* **8**, 3494–3511 (2020).
20. Marten, E., Müller, R.-J. & Deckwer, W.-D. Studies on the enzymatic hydrolysis of polyesters. II. Aliphatic–aromatic copolyesters. *Polym. Degrad. Stab.* **88**, 371–381 (2005).
21. Ellis, L. D. et al. Chemical and biological catalysis for plastics recycling and upcycling. *Nat. Catal.* **4**, 539–556 (2021).
22. Gould, S. M. & Tawfik, D. S. Directed evolution of the promiscuous esterase activity of carbonic anhydrase II. *Biochemistry* **44**, 5444–5452 (2005).
23. Bigley A. N. & Raushel F. M. The evolution of phosphotriesterase for decontamination and detoxification of organophosphorus chemical warfare agents. *Chem. Biol. Interact.* **308**, 80–88 (2019).
24. Studer, S. et al. Evolution of a highly active and enantiospecific metalloenzyme from short peptides. *Science* **362**, 1285–1288 (2018).
25. Schwizer, F. et al. Artificial metalloenzymes: Reaction scope and optimization strategies. *Chem. Rev.* **118**, 142–231 (2018).
26. Hoffnagle, A. M. & Tezcan, F. A. Atomically accurate design of metalloproteins with predefined coordination geometries. *J. Am. Chem. Soc.* **145**, 14208–14214 (2023).
27. Braun, M. et al. Computational enzyme design by catalytic motif scaffolding. Preprint at *bioRxiv* https://doi.org/10.1101/2024.08.02.606416 (2025).
28. Hossack, E. J, Hardy, F. J & Green, A. P Building enzymes through design and evolution. *ACS Catal.* **13**, 12436–12444 (2023).
29. Ming, Y. et al. A review of enzyme design in catalytic stability by artificial intelligence. *Brief. Bioinformatics* **24**, bbad065 (2023).
30. Ahern, W. et al. Atom level enzyme active site scaffolding using RFdiffusion2. *Nat. Methods* https://doi.org/10.1038/s41592-025-02975-x (in the press).

31. Lipman, Y., Chen, R. T. Q., Ben-Hamu, H., Nickel, M. & Le, M. Flow matching for generative modeling. in *The Eleventh International Conf. on Learning Representations* https://openreview.net/forum?id=PqvMRDCJT9t (2022).
32. Yim, J. et al. Improved motif-scaffolding with SE(3) flow matching. *Trans. Mach. Learn. Res.* https://openreview.net/forum?id=fa1ne8xDGn (2024).
33. Tantillo, D. J. & Houk, K. N. in *Stimulating Concepts in Chemistry* (eds Stoddart, J. F. & Shibasaki, M.) 79–88 (Wiley, 2005).
34. Dauparas, J. et al. Robust deep learning-based protein sequence design using ProteinMPNN. *Science* **378**, 49–56 (2022).
35. Jumper, J. et al. Highly accurate protein structure prediction with AlphaFold. *Nature* **596**, 583–589 (2021).
36. Dauparas, J. et al. Atomic context-conditioned protein sequence design using LigandMPNN. *Nat. Methods* **22**, 717–723 (2025).
37. Tyka, M. D. et al. Alternate states of proteins revealed by detailed energy landscape mapping. *J. Mol. Biol.* **405**, 607–618 (2011).
38. Zhang, Y. & Skolnick, J. Scoring function for automated assessment of protein structure template quality. *Proteins* **57**, 702–710 (2004).
39. Der, B. S. et al. Metal-mediated affinity and orientation specificity in a computationally designed protein homodimer. *J. Am. Chem. Soc.* **134**, 375–385 (2012).
40. Kiefer, L. L. & Fierke, C. A. Functional characterization of human carbonic anhydrase II variants with altered zinc binding sites. *Biochemistry* **33**, 15233–15240 (1994).
41. Coleman, J. E. & Vallee, B. L. Metallocarboxypeptidases. *J. Biol. Chem.* **235**, 390–395 (1960).
42. Feder, J., Garrett, L. R. & Kochavi, D. Studies on the inhibition of neutral proteases by 1,10-phenanthroline. *Biochim. Biophys. Acta* **235**, 370–377 (1971).
43. Felici, A. et al. An overview of the kinetic parameters of class B β-lactamases. *Biochem. J* **291**, 151–155 (1993).
44. Verpoorte, J. A., Mehta, S. & Edsall, J. T. Esterase activities of human carbonic anhydrases B and C. *J. Biol. Chem.* **242**, 4221–4229 (1967).
45. Stöcker, W., Sauer, B. & Zwilling, R. Kinetics of nitroanilide cleavage by astacin. *Biol. Chem.* **372**, 385–392 (1991).
46. Stoczko, M., Frère, J.-M., Rossolini, G. M. & Docquier, J.-D. Functional diversity among metallo-beta-lactamases: characterization of the CAR-1 enzyme of *Erwinia carotovora*. *Antimicrob. Agents Chemother.* **52**, 2473–2479 (2008).
47. Mascarenhas, R. et al. Structural and biochemical characterization of AidC, a quorum-quenching lactonase with atypical selectivity. *Biochemistry* **54**, 4342–4353 (2015).

Reporting summary

Further information on research design is available in the Nature Portfolio Reporting Summary linked to this article.

Data availability

All data are available in the main text or as supplementary materials, including the DFT coordinates of the theozymes from each design campaign (Supplementary Data 1), the ordered protein sequences from each design campaign (Supplementary Data 2) and the design models of the ordered sequences from each design campaign (Supplementary Data 3). For gel source data, see Supplementary Fig. 27. Protein crystal structure coordinates and structure factors are available in the Protein Data Bank with PDB IDs 9PYJ (apo ZETA_2) and 9PYL (Zn(II)-bound ZETA_2).

Code availability

RFdiffusion2 is publicly available on GitHub at https://github.com/RosettaCommons/RFdiffusion2. PLACER is publicly available on GitHub at https://github.com/baker-laboratory/PLACER. Other design scripts and JupyterHub notebooks of the design pipelines used to design metallohydrolases are publicly available on GitHub at https://github.com/baker-laboratory/Metallohydrolase_Enzyme_Design.

Acknowledgements We thank Y. Wang, A. Hunt, J. Gershon, J. Min, C. Demakis, A. Shida and Y. Kipnis for discussions about zinc hydrolases; A. Swartz, P. Lund-Anderson, N. Ennist, Y. Hsia, S. Sharma and S. Honda for valuable discussions about metal binding, small molecule binding, and general discussions about protein design; D. Evans for guidance with performing quantum chemistry; M. Bauer for software assistance; K. VanWormer, R. Ticzon and H. Nunez-Ortega for managing the wet laboratory resources; and L. Goldschmidt for maintaining the computational resources at the Institute for Protein Design. This work was funded by the National Science Foundation Graduate Research Fellowship Program, grant no. DGE-2140004 (S.M.W.), the Defense Advanced Research Projects Agency, Cooperative Agreement HR00112520029, CFDA no. 12.910 (S.M.W., D.K., S.J.P. and D.B.), The Howard Hughes Medical Institute (D.B. and I.K.), The Audacious Project at the Institute for Protein Design (A.L. and N.H.), The Open Philanthropy Project Improving Protein Design Fund (I.K. and S.J.P.), the ETH Zurich (D.H.), The Bill and Melinda Gates Foundation INV-010680 (D.K. and W.A.), and the Schmidt Futures Foundation (A.L., S.J.P. and S.S.). Crystallographic data collection was performed on APS NE-CAT 24ID-E beamline and the beam time award(s) (https://doi.org/10.46936/APS-190193/60014259) from the Advanced Photon Source, a US Department of Energy (DOE) Office of Science user facility operated for the DOE Office of Science by Argonne National Laboratory under contract no. DE-AC02-06CH11357.

Author contributions S.M.W., I.K. and D.B. conceptualized the metallohydrolase design project. W.A., D.T. and D.B. conceptualized RFdiffusion2. W.A., J.Y., D.T., S.S. and R.K. contributed to the development of RFdiffusion2. W.A. trained all versions of RFdiffusion2 used in the study. S.M.W. and I.K. performed DFT calculations. S.M.W., I.K. and D.K. developed the computational design pipeline. S.J.P. and A.L. contributed ideas, code and functions. S.M.W. and D.K. produced and characterized the designs and analysed the results. N.H. performed the Zn(II)-binding affinity experiments. A.K., E.J. and A.K.B. performed protein crystallography. I.K., S.J.P., A.L. and D.H. provided guidance for optimizing experimental protocols and helped to interpret key results. D.B. and D.H. supervised the research. The manuscript and supplementary information were drafted by S.M.W., D.K., I.K. and D.B. All authors reviewed and commented on the manuscript.

Competing interests The authors declare no competing interests.

Additional information

Supplementary information The online version contains supplementary material available at https://doi.org/10.1038/s41586-025-09746-w.

Correspondence and requests for materials should be addressed to Indrek Kalvet, Donald Hilvert or David Baker.

Peer review information *Nature* thanks Adrian Mulholland, M. Elizabeth Stroupe and the other, anonymous, reviewer(s) for their contribution to the peer review of this work. Peer reviewer reports are available.

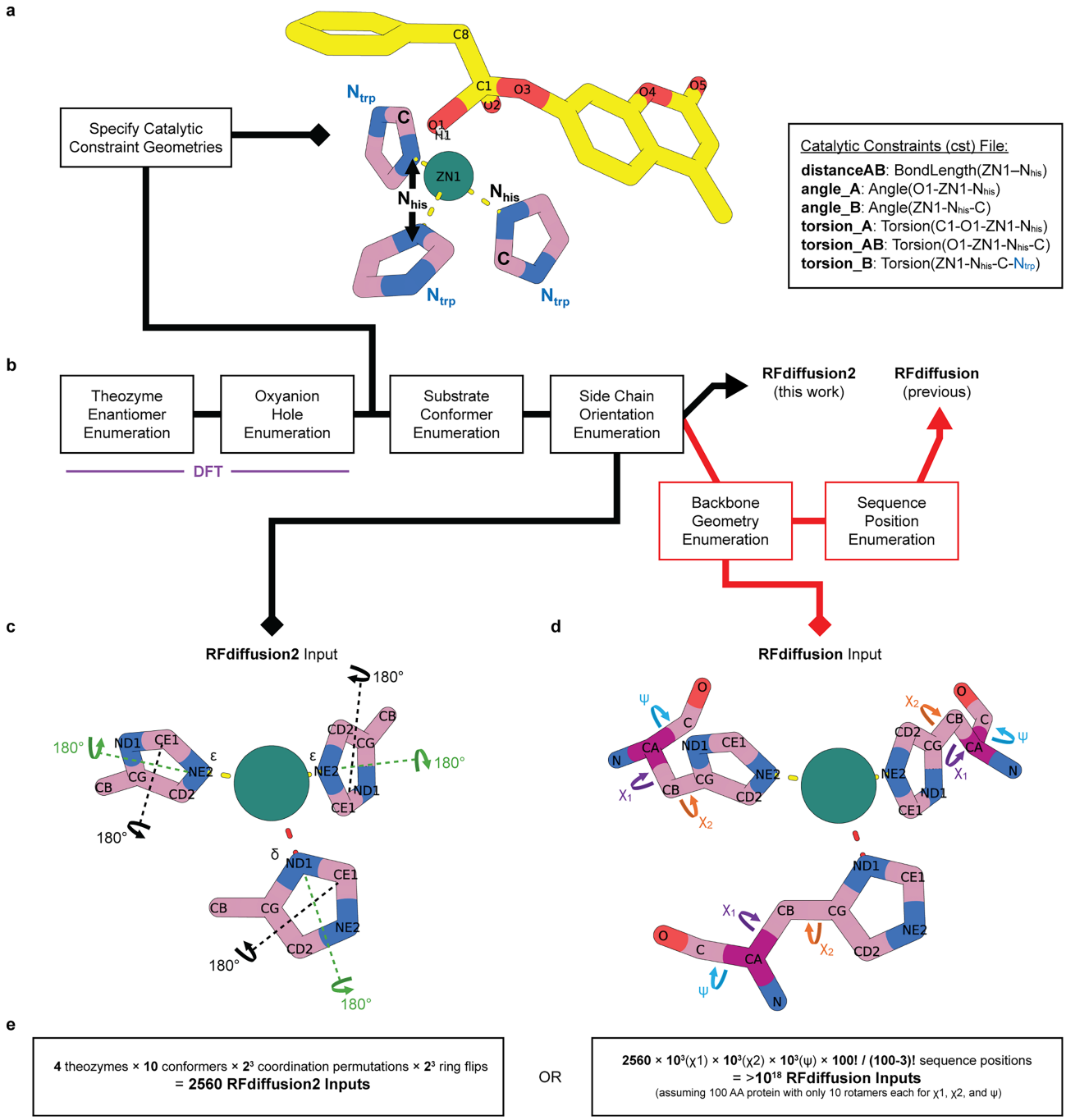

Extended Data Fig. 1 | Catalytic constraints and enumerative catalytic motif scaffolding around theozymes for RFdiffusion2 compared to RFdiffusion. **a**, Example theozyme from DFT with relevant ligand atoms labeled and Rosetta constraint file labeling for the histidine side chains. Catalytic constraint files specifying the coordination geometry of the histidines were created at this step for each of the 4 theozymes from DFT. Note that N_{his} is a general Rosetta label that accommodates epsilon and delta coordination geometries with zinc. **b**, Theozyme sampling enumeration pipeline with diverging paths for RFdiffusion2 and RFdiffusion. **c**, Side chain enumeration sampling different combinations of zinc coordination and imidazole orientations. Note that there are only 64 permutations of coordination and Cβ positioning. **d**, Backbone enumeration for RFdiffusion. This is required in addition to the sampling in (**c**). **e**, Calculation of the total number of possible RFdiffusion2 and RFdiffusion inputs. It should be noted that not all combinations of rotamers and sequence positions will be viable, somewhat reducing the total number, but to nowhere near the tiny enumeration space needed for RFdiffusion2.

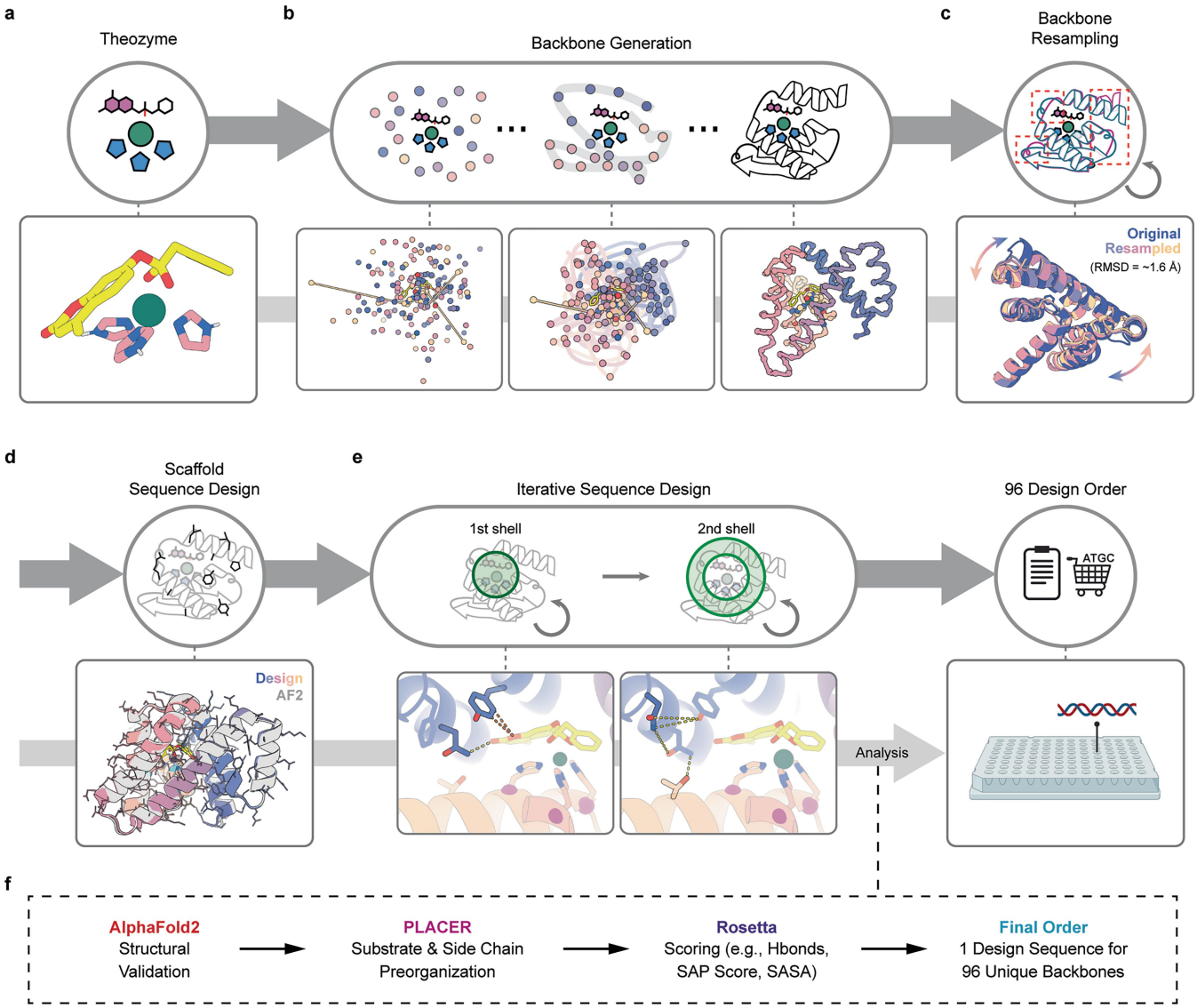

Extended Data Fig. 2 | Computational design pipeline for metallohydrolases. a-f, Visual illustrations of the key steps in the computational design pipeline, with examples showing A1 (ZETA_1) at each stage in the pipeline.

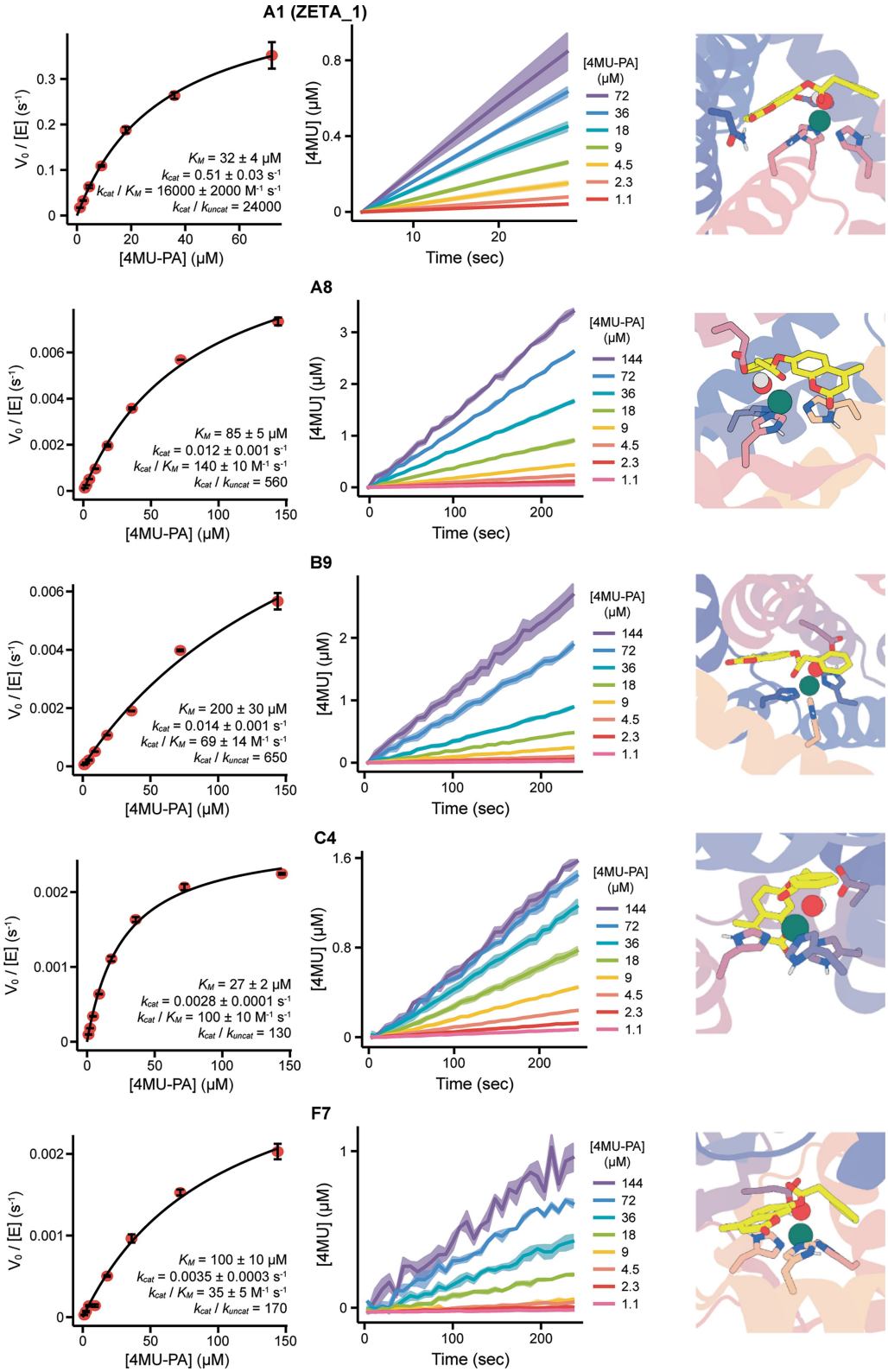

Extended Data Fig. 3 | Michaelis-Menten kinetic characterization of the five design hits from the first design campaign. Michaelis-Menten plots from these data are shown on the left. The progress curves for the measured initial velocities are shown in the middle. Designed active sites with the histidines and general base are displayed on the right.

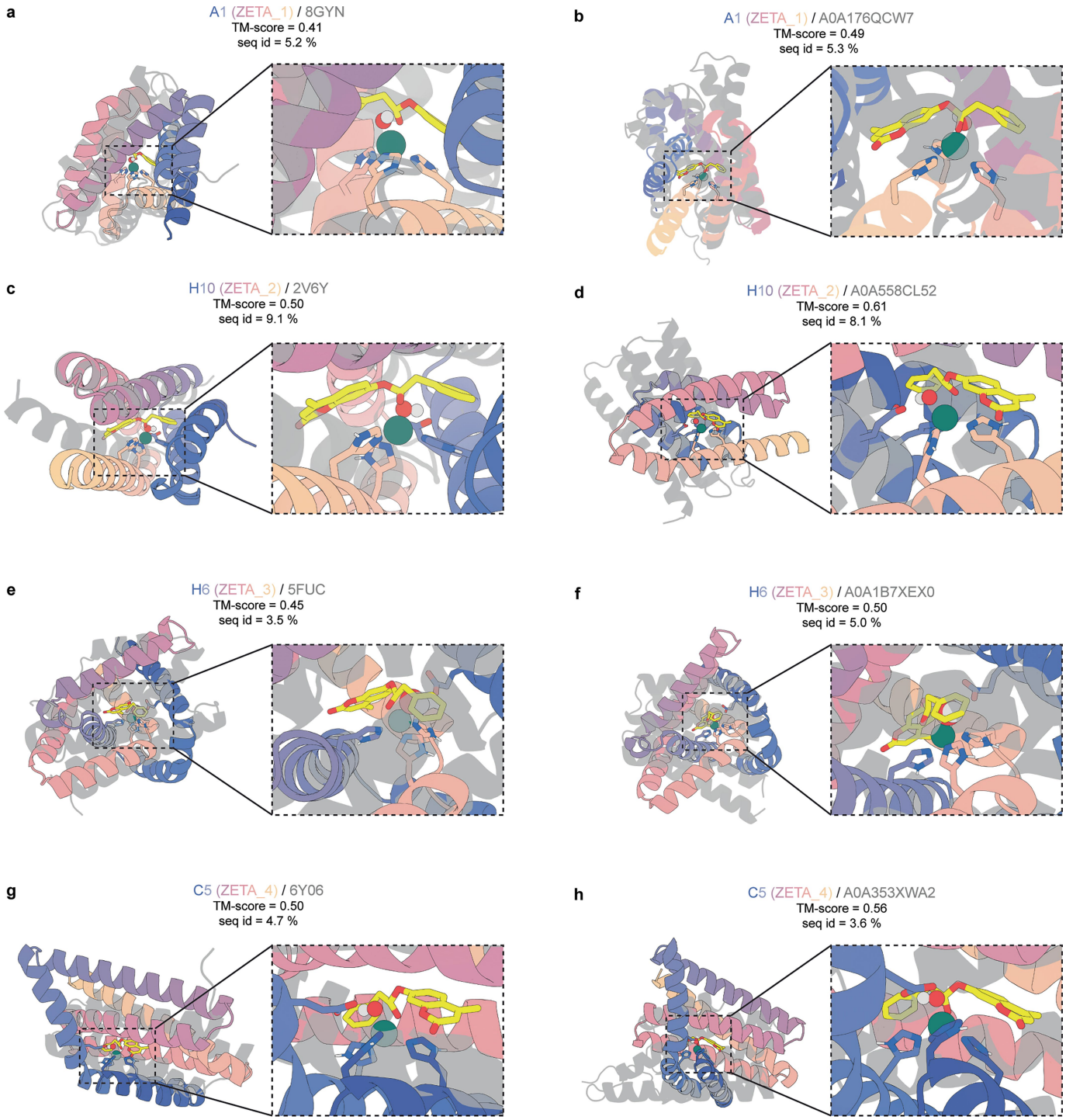

Extended Data Fig. 4 | Structural novelty of the ZETA_1-4 designs. Global Cα alignment of the ZETA_1-4 design models with their most similar structures in the Protein Data Bank and AlphaFold2 Database based on TM-score, respectively. **a**,**b**, ZETA_1 aligned with (**a**) PDB structure 8GYM and (**b**) AF2 prediction A0A176QCW7. **c**,**d**, ZETA_2 aligned with (**c**) PDB structure 2V6Y and (**d**) AF2 prediction A0A558CL52. **e**,**f**, ZETA_3 aligned with (**e**) PDB structure 5FUC and (**f**) AF2 prediction A0A1B7XEX0. **g**,**h**, ZETA_4 aligned with (**g**) PDB structure 6Y06 and (**h**) AF2 prediction A0A353XWA2. In all cases, the designed proteins are shown in a colour gradient, and the PDB/AF2 structures are shown in grey. The poor alignment, low sequence identity, and modest TM-scores highlight the novelty of these de novo scaffolds.

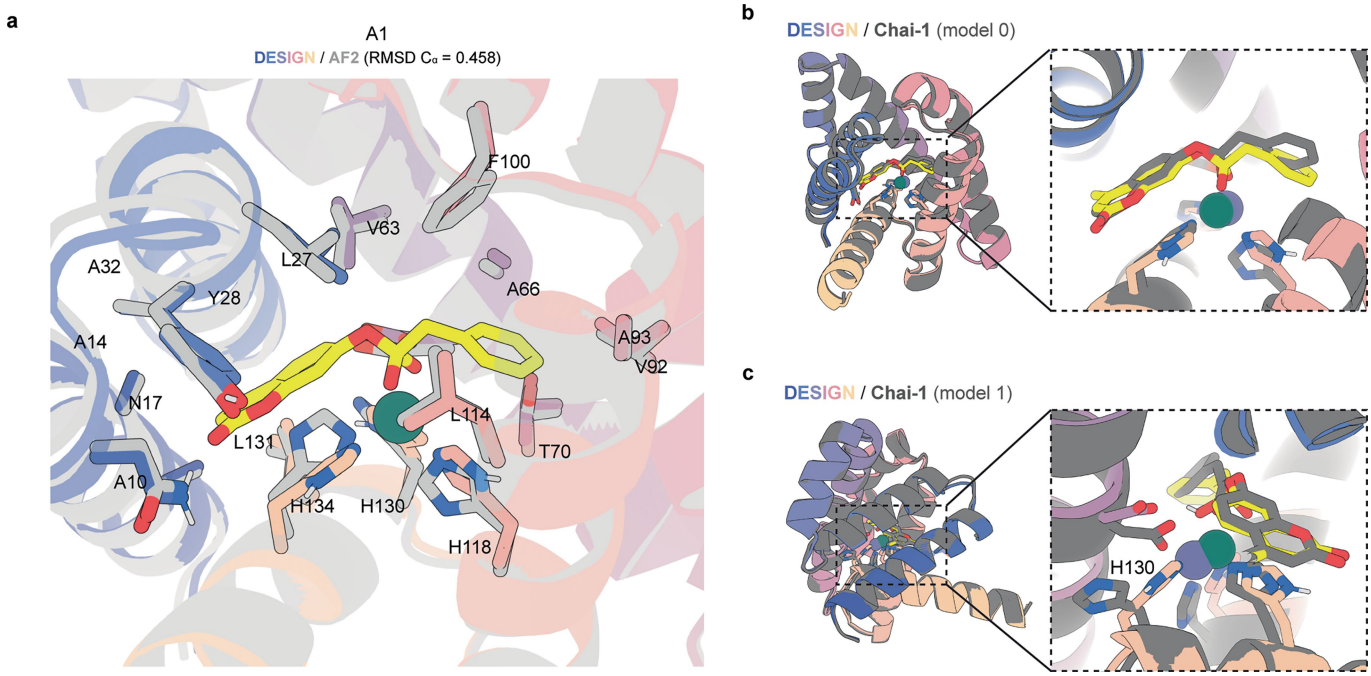

Extended Data Fig. 5 | Predicted structures of the A1 (ZETA_1) design. **a**, Active site of the A1 design model with pocket residues labeled. Designed structure is coloured and AlphaFold2 apo-predicted structure is grey. The structures are in high agreement, suggesting that A1 has a high degree of preorganization. **b**, Global and active site comparison of the A1 design (colored) with model 0 of the Chai-1[28] structure sequence/scaffold) with Zn(II) and 4MU-PA. The substrate SMILES file was provided to Chai-1, not the tetrahedral intermediate, whereas the A1 design model contains the transition state of the nucleophilic attack of hydroxide to the substrate. The global scaffold fold prediction by Chai-1 is nearly identical to the design model scaffold (r.m.s.d. Cα = 0.413). Additionally, the zinc and substrate docking positions by Chai-1 are nearly identical to the design model; model 0 of Chai-1 also predicts the zinc being coordinated by the 3 histidines (H118, H130, H134) in nearly the same orientations as the design model. **c**, Global and active site comparison of the A1 design model (coloured) with model 1 of the Chai-1 structural prediction (grey) in the presence of zinc and 4MU-PA. Note this is shown from the side/back view. Again, the global scaffold fold prediction and substrate docking position by Chai-1 are nearly identical to the design model. Interestingly, Chai-1 predicts a slightly different zinc docking position in model 1 with H130 flipped away from the active site, and D67 is instead coordinating zinc with the other two histidines (H118 and H134). This supports the hypothesis that H130 and D67 are competitively binding zinc, explaining the results observed from the mutant activity and zinc binding experiments. Thus, it is unlikely that D67 is functioning efficiently, if at all, as a general base, providing a rational starting point for potential redesign.

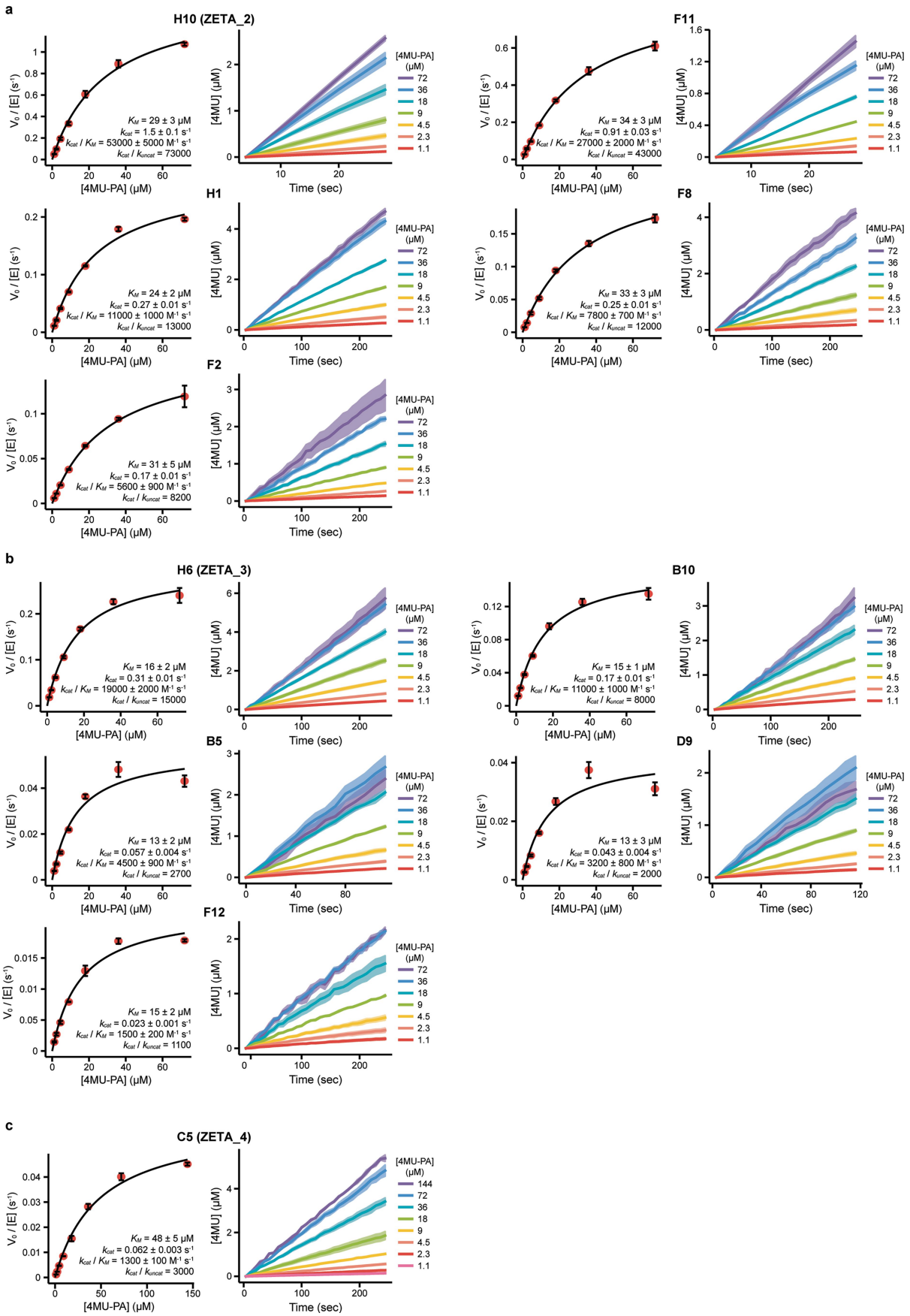

Extended Data Fig. 6 | Michaelis-Menten kinetics of eleven major hits from the second design campaign. a-c, Kinetics of designs grouped by (**a**) ZETA_2 scaffold, (**b**) ZETA_3 scaffold, and (**c**) ZETA_4 scaffold.

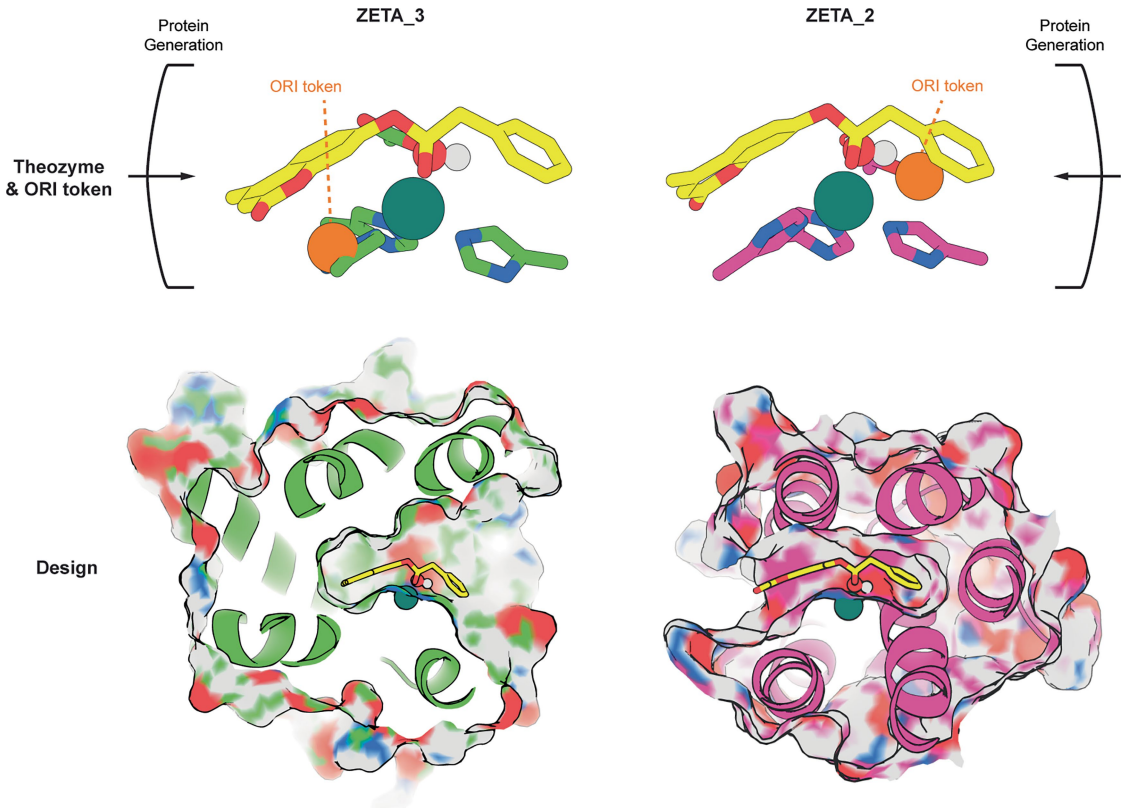

Extended Data Fig. 7 | Opposite substrate binding modes in ZETA_2 and ZETA_3 design models result from ORI placement. The ORI token is an optional coordinate fed to the updated RFdiffusion2, which instructs the model on where it should aim to generate the protein center of mass (Supplementary Methods 4.2). Thus, the ORI token can be used to specify which parts of the substrate/theozyme should be more surrounded by protein (buried) on average. ZETA_2 (right) and ZETA_3 (left) are designed to bind the substrate in opposite orientations; this arose from the opposite placement of ORI tokens with respect to the substrate. The bottom panels show a cross-section of the design models for these enzymes with the surface view to observe the designed substrate binding pocket. In ZETA_3 (left) the PA is solvent-exposed and the 4MU is buried because the ORI token is next to the 4MU. In ZETA_2 (right) the 4MU is solvent-exposed and the PA is buried because the ORI token is next to the PA.

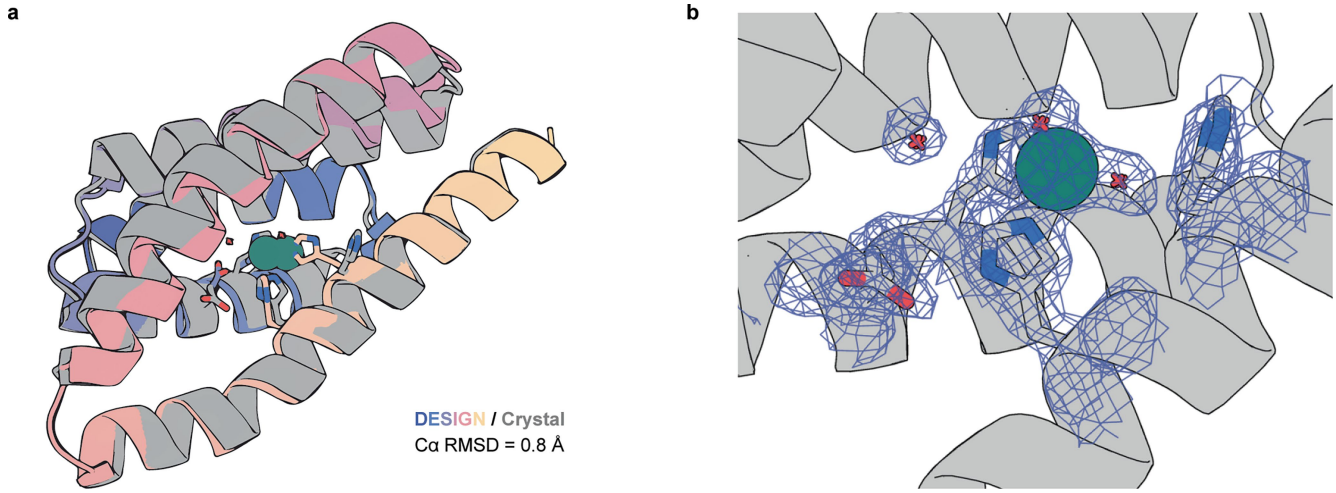

Extended Data Fig. 8 | Crystal structure of Zn(II)-bound ZETA_2 after soaking. a, Cα superposition of the design model and the X-ray crystal structure of ZETA_2 (PDB: 9PYL) in the Zn(II)-bound state from crystal soaking, resolved at 2.1 Å resolution. Catalytic residues shown as sticks and Zn(II) ions shown as green spheres. The structures are in close agreement (Cα r.m.s.d. = 0.8 Å) and the Zn(II) ion is present with 100% occupancy in the correct binding location (r.m.s.d. = 1.7 Å). **b**, Active site close-up view with the 2mFobs-DFcalc electron-density map (blue mesh) contoured at 1.0 σ for the catalytic residues, Zn(II) ion, and water molecules. Surprisingly, one of the catalytic histidines (H110) is flipped out in the experimental structure to interact with a Zn(II) ion in solution, likely because of the high Zn(II) concentration used in the crystal-soaking buffer. We hypothesize that this may be an intermediate conformational state relevant to Zn(II)-binding that was captured and stabilized in the crystal. Additionally, the catalytic base (E34) adopts a different conformation from the catalytic conformation in this crystal structure; however, conformational flexibility for this residue was also observed in the apo-ZETA_2 crystal structure, with one of the conformations being the catalytic conformation (Fig. 5b). These conformations for E34 and H110 could be artifacts from the crystallization and soaking process or may suggest that ZETA_2 has dynamic properties. If it is dynamic, this poses an interesting question of whether the dynamics accelerate or hinder the activity of ZETA_2. Future work could try to buttress these residues with redesign or new de novo scaffolds to investigate if this would increase or decrease activity. Crystal structure shown in grey and design model shown in colour in all panels.

Extended Data Table 1 | Michaelis-Menten parameters for the hydrolysis of 4MU-PA by the designed de novo metallohydrolases and mutants

Variant	k_{cat}/K_M (M^{-1} s^{-1})	k_{cat} (s^{-1})	K_M (μM)
1st Design Campaign			
A1 (ZETA_1)	16000 ± 2000	0.51 ± 0.03	32 ± 4
A8	140 ± 10	0.012 ± 0.001	85 ± 5
B9	69 ± 14	0.014 ± 0.001	200 ± 30
C4	100 ± 10	0.0028 ± 0.0001	27 ± 2
F7	35 ± 5	0.0035 ± 0.0003	100 ± 10
A1 (ZETA_1) Knockout Mutants			
A1 H130A	1300 ± 100	0.020 ± 0.001	16 ± 2
A1 N17A	2000 ± 100	0.031 ± 0.001	16 ± 1
A1 D67A	14000 ± 2000	0.17 ± 0.01	12 ± 1
A1 H118A	Inactive	Inactive	Inactive
A1 H134A	Inactive	Inactive	Inactive
A1 H118A;H130A;H134A	Inactive	Inactive	Inactive
2nd Design Campaign			
H10 (ZETA_2)	53000 ± 5000	1.5 ± 0.1	29 ± 3
F11	27000 ± 2000	0.91 ± 0.03	34 ± 3
H1	11000 ± 1000	0.27 ± 0.01	24 ± 2
F8	7800 ± 700	0.25 ± 0.01	33 ± 3
F2	5600 ± 900	0.17 ± 0.01	31 ± 5
H6 (ZETA_3)	19000 ± 2000	0.31 ± 0.01	16 ± 2
B10	11000 ± 1000	0.17 ± 0.01	15 ± 1
B5	4500 ± 900	0.057 ± 0.004	13 ± 2
D9	3200 ± 800	0.043 ± 0.004	13 ± 3
F12	1500 ± 200	0.023 ± 0.001	15 ± 2
C5 (ZETA_4)	1100 ± 200	0.081 ± 0.006	73 ± 9

Extended Data Table 2 | Crystallography data collection and refinement statistics

	***Apo*-ZETA_2** PDB Code: 9PYJ	**Zn(II)-bound ZETA_2** PDB Code: 9PYL
Data collection		
Space group	P 2_1	P 2_1 2_1 2_1
Cell dimensions		
a, *b*, *c* (Å)	42.21, 94.86, 50.38	42.71, 52.62, 98.86
α, β, γ (˚)	90, 90, 90	90, 90, 90
Resolution (Å)	94.86 - 3.49 (3.82 - 3.49) *	98.86 - 2.07 (2.13 - 2.07)
R_{sym} or R_{merge}	0.335 (0.935)	0.499 (1.418)
I / σI	3.2 (1.8)	7.6 (2.1)
Completeness (%)	99.0 (99.5)	99.5 (99.2)
Redundancy	6.7 (6.7)	12.4 (12.4)
Refinement		
Resolution (Å)	50.38 - 3.49 (3.82 - 3.49)	49.43 - 2.07 (2.23 - 2.07)
No. reflections	4863	13975
R_{work} / R_{free}	0.2287 (0.2369) / 0.2831 (0.2951)	0.2414 (0.2607) / 0.2950 (0.3561)
No. atoms		
Protein	3955	2002
Ligand/ion	n/a	3
Water	n/a	70
B-factors		
Protein	89	26
Ligand/ion	n/a	42
Water	n/a	30
R.m.s. deviations		
Bond lengths (Å)	0.008	0.003
Bond angles (°)	1.47	0.47

*Single xtal used for each data/structure. *Values in parentheses are for highest-resolution shell.

nature portfolio

Corresponding author(s): Indrek Kalvet, Donald Hilvert, David Baker

Last updated by author(s): Oct 8, 2025

Reporting Summary

Nature Portfolio wishes to improve the reproducibility of the work that we publish. This form provides structure for consistency and transparency in reporting. For further information on Nature Portfolio policies, see our Editorial Policies and the Editorial Policy Checklist.

Statistics

For all statistical analyses, confirm that the following items are present in the figure legend, table legend, main text, or Methods section.

n/a	Confirmed	
☐	☒	The exact sample size (*n*) for each experimental group/condition, given as a discrete number and unit of measurement
☐	☒	A statement on whether measurements were taken from distinct samples or whether the same sample was measured repeatedly
☐	☒	The statistical test(s) used AND whether they are one- or two-sided *Only common tests should be described solely by name; describe more complex techniques in the Methods section.*
☒	☐	A description of all covariates tested
☒	☐	A description of any assumptions or corrections, such as tests of normality and adjustment for multiple comparisons
☐	☒	A full description of the statistical parameters including central tendency (e.g. means) or other basic estimates (e.g. regression coefficient) AND variation (e.g. standard deviation) or associated estimates of uncertainty (e.g. confidence intervals)
☐	☒	For null hypothesis testing, the test statistic (e.g. *F*, *t*, *r*) with confidence intervals, effect sizes, degrees of freedom and *P* value noted *Give P values as exact values whenever suitable.*
☒	☐	For Bayesian analysis, information on the choice of priors and Markov chain Monte Carlo settings
☒	☐	For hierarchical and complex designs, identification of the appropriate level for tests and full reporting of outcomes
☒	☐	Estimates of effect sizes (e.g. Cohen's *d*, Pearson's *r*), indicating how they were calculated

Our web collection on statistics for biologists contains articles on many of the points above.

Software and code

Policy information about availability of computer code

Data collection

The Rosetta macromolecular modeling suite (https://rosettacommons.org/) is freely available to academic and non-commercial users. Commercial licenses for the suite are available through the University of Washington Technology Transfer Office.

All the data in this study was experimentally measured or computationally generated in the design pipeline created by the authors, which will be available open-source on GitHub upon publication of the manuscript. No external data was acquired.

Code for the computational design of metallohydrolases will be made available upon acceptance of the manuscript at the following repository:
https://github.com/baker-laboratory/Metallohydrolase_Enzyme_Design

The manuscript describing the training and benchmarking of RFdiffusion2 has now been posted in the bioRxiv (Ahern et al. bioRxiv 2025) and has been submitted to Nature Methods. Please refer to the link: https://www.biorxiv.org/content/10.1101/2025.04.09.648075v2. The associated code and pretrained neural network weights are available at:
https://github.com/RosettaCommons/RFdiffusion2

PLACER is publicly available on GitHub at the link: https://github.com/baker-laboratory/PLACER.

Data analysis	The molecular mass of each protein was deconvoluted by Bioconfirm software (10.0) using a total entropy algorithm. Data were analyzed and plotted using Python 3.12; analysis was done using numpy 1.26.4 and pandas 2.2.2 and plotting was done using seaborn 0.13.2 and matplotlib 3.9.2.

For manuscripts utilizing custom algorithms or software that are central to the research but not yet described in published literature, software must be made available to editors and reviewers. We strongly encourage code deposition in a community repository (e.g. GitHub). See the Nature Portfolio guidelines for submitting code & software for further information.

Data

Policy information about availability of data

All manuscripts must include a data availability statement. This statement should provide the following information, where applicable:

- Accession codes, unique identifiers, or web links for publicly available datasets
- A description of any restrictions on data availability
- For clinical datasets or third party data, please ensure that the statement adheres to our policy

Source data for the figures will be made available online upon publication of this manuscript. Gene sequences will be deposited to GenBank upon publication of this manuscript. Design models are available for peer-review in the supplemental information and will be made publicly available upon publication of this manuscript. Codon-optimized plasmids that were used in the study will be made publicly available through Addgene upon publication of this manuscript.

Research involving human participants, their data, or biological material

Policy information about studies with human participants or human data. See also policy information about sex, gender (identity/presentation), and sexual orientation and race, ethnicity and racism.

Reporting on sex and gender	No research involving human participants was conducted in this study. Not applicable.
Reporting on race, ethnicity, or other socially relevant groupings	No research involving human participants was conducted in this study. Not applicable.
Population characteristics	No research involving human participants was conducted in this study. Not applicable.
Recruitment	No research involving human participants was conducted in this study. Not applicable.
Ethics oversight	No research involving human participants was conducted in this study. Not applicable.

Note that full information on the approval of the study protocol must also be provided in the manuscript.

Field-specific reporting

Please select the one below that is the best fit for your research. If you are not sure, read the appropriate sections before making your selection.

☒ Life sciences ☐ Behavioural & social sciences ☐ Ecological, evolutionary & environmental sciences

For a reference copy of the document with all sections, see nature.com/documents/nr-reporting-summary-flat.pdf

Life sciences study design

All studies must disclose on these points even when the disclosure is negative.

Sample size	No statistical methods were used to pre-determine the sample sizes in this study. The number of designs we ordered for screening (192) corresponds to the number of DNA fragments that can fit on a single commercial eBlock synthesized by IDT.
Data exclusions	No sample was excluded from the data analysis.
Replication	Measurements for protein concentration were performed in triplicate. All standard curves were measured in triplicate and used on the same day as experiments. Measurements of enzyme kinetics were done in triplicate and replicated with biological duplicates. During analysis of the purification protocol for the best enzyme designs (ZETA1-4), Coomassie-stained SDS PAGE gels were done in duplicate, which is reflected in a supplemental figure in the supplemental information. Zinc affinity measurements were done in duplicates. Circular dichroism measurements were performed in duplicates. Measurements of the lower bound for the total enzyme turnover were measured in triplicate. Size exclusion chromatography was at least repeated in biological duplicates.
Randomization	No randomization was used in this study.
Blinding	The author performing the zinc affinity measurements was blinded to the sample type. Researchers were not blinded for any other experiments.

Reporting for specific materials, systems and methods

We require information from authors about some types of materials, experimental systems and methods used in many studies. Here, indicate whether each material, system or method listed is relevant to your study. If you are not sure if a list item applies to your research, read the appropriate section before selecting a response.

Materials & experimental systems

n/a	Involved in the study
☒	☐ Antibodies
☒	☐ Eukaryotic cell lines
☒	☐ Palaeontology and archaeology
☒	☐ Animals and other organisms
☒	☐ Clinical data
☒	☐ Dual use research of concern
☒	☐ Plants

Methods

n/a	Involved in the study
☒	☐ ChIP-seq
☒	☐ Flow cytometry
☒	☐ MRI-based neuroimaging

Plants

Seed stocks	No research involving plants was conducted in this study. Not applicable.
Novel plant genotypes	No research involving plants was conducted in this study. Not applicable.
Authentication	No research involving plants was conducted in this study. Not applicable.